Accepted Manuscript

Synchronisation under shocks: The Lévy Kuramoto model

Dale Roberts, Alexander C. Kalloniatis

PII: S0167-2789(17)30306-8
DOI: https://doi.org/10.1016/j.physd.2017.12.005
Reference: PHYSD 31986

To appear in: *Physica D*

Received date : 2 June 2017
Revised date : 2 December 2017
Accepted date : 4 December 2017

Please cite this article as: D. Roberts, A.C. Kalloniatis, Synchronisation under shocks: The Lévy Kuramoto model, *Physica D* (2017), https://doi.org/10.1016/j.physd.2017.12.005

Synchronisation Under Shocks: the Lévy Kuramoto Model

Dale Roberts[a], Alexander C. Kalloniatis[b]

[a]*Australian National University*
Canberra, Australia, 2601
[b]*Defence Science and Technology Group,*
Canberra, Australia 2600

Abstract

We study the Kuramoto model of identical oscillators on Erdős-Rényi (ER) and Barabasi-Alberts (BA) scale free networks examining the dynamics when perturbed by a Lévy noise. Lévy noise exhibits heavier tails than Gaussian while allowing for their tempering in a controlled manner. This allows us to understand how 'shocks' influence individual oscillator and collective system behaviour of a paradigmatic complex system. Skewed α-stable Lévy noise, equivalent to fractional diffusion perturbations, are considered, but overlaid by exponential tempering of rate λ. In an earlier paper we found that synchrony takes a variety of forms for identical Kuramoto oscillators subject to stable Lévy noise, not seen for the Gaussian case, and changing with α: a noise-induced drift, a smooth α dependence of the point of cross-over of synchronisation point of ER and BA networks, and a severe loss of synchronisation at low values of α. In the presence of tempering we observe both analytically and numerically a dramatic change to the $\alpha < 1$ behaviour where synchronisation is sustained over a larger range of values of the 'noise strength' σ, improved compared to the $\alpha > 1$ tempered cases. Analytically we study the system close to the phase synchronised fixed point and solve the tempered fractional Fokker-Planck equation. There we observe that densities show stronger support in the basin of attraction at low α for fixed coupling, σ and tempering λ. We then perform numerical simulations for networks of size $N = 1000$ and average degree $\bar{d} = 10$. There, we compute the order parameter r as a function of σ for fixed α and λ and observe values of $r \approx 1$ over larger ranges of σ for $\alpha < 1$ and $\lambda \neq 0$. In addition we observe drift of both positive and negative slopes for different α and λ when native frequencies are equal, and confirm a sustainment of synchronisation down to low values of α. We propose a mechanism for this in terms of the basic shape of the tempered stable Lévy densities for various α and how it feeds into Kuramoto oscillator dynamics and illustrate this with examples of specific paths.

1. Introduction

The dynamical system of oscillators proposed by Kuramoto [1] provides a way to understand some of the complexities of spontaneous synchronisation inherent to some real-world complex systems of physical, biological, or social nature. The original model captures structure and rhythmic behaviour. Generalising the all-to-all case to non-complete networks [2, 3, 4, 5] and subjecting oscillators to noisy Gaussian perturbations [2, 6, 7, 8] or heavier-tailed perturbations [9] offers further applicability.

In this paper we examine the relationship between synchronisation of oscillators and the speed of decay in the tails of the noise distribution that seeks to disrupt their collective behaviour. As such, we perturb each oscillators by a Lévy process, a natural generalisation of Brownian motion, that allows heavier tails in the distribution of the process increments. More precisely, we use a tempered stable process so that we can control the rate of tail decay to demonstrate a striking relationship between this rate and the onset of synchronisation within the system.

The main motivation of this study lies in the viability of a Lévy Kuramoto model as a representation of social processes or distributed decision-making [10, 11, 12, 13]. Human cognitive processes are known to be cyclic [14], noisy [15] and involve leaps of intuition in complex problem solving [16] or recognition of previously experienced patterns, known as 'priming' [17, 18]. Modelling these leaps by a Lévy process enables quantification of these otherwise qualitative models. Additionally, recent results in the field

of brain research show that heavy tails in the distributions of alpha and beta rhythms [19] can be observed which lends further weight to heavy-tailed dynamics proposed in this paper. Additional motivations are more practical. First, introducing leaps into the Kuramoto model using a stable process (i.e., fractional diffusion) makes most moments of the distribution ill-defined so that matching to empirical data is fraught. The addition of tempering softens this behaviour so that all moments of the process are finite, while still generalising away from Gaussianity. Tempered stable processes allow us to understand how leaps influence synchronisation dynamics but in a model that can be fitted to data from real-world systems where empirical moments will always be finite. Second, by tuning the decay parameter we are able to probe the basin of attraction of the Kuramoto system.

It is well understood that network topology plays an important role in synchronisation [20, 21, 22, 23, 24, 25]. The key insight is that scale-free graphs, such as that of Barabasi and Alberts (BA), have lower critical coupling than Erdös-Renyi (ER) graphs. However, comparing the topologies at a fixed size, the latter encourages faster synchronisation as the coupling strength increases beyond the critical coupling value. Therefore, for completeness, we also explore the difference in robustness of the dynamics under these two topologies when tempered stable noise is introduced.

2. The model

In the most general case, we consider a nonlinearly coupled model perturbed by a Lévy process written as the system of N stochastic differential equations (SDEs) given for each $i \in \{1,\dots,N\}$ by

$$\mathrm{d}\theta_i(t) = \omega_i\,\mathrm{d}t - \frac{K}{N}\sum_{j=1}^{N} A_{ij} H(\theta_i(t)-\theta_j(t))\mathrm{d}t + \mathrm{d}L_i(t), \tag{1}$$

with $\theta_i(0) = x_i$ where θ_i is the time-dependent phase angle at vertex $v_i \in V$ of the connected graph $\mathcal{G} = (V,E)$ of size N. The topology of the graph is encoded in the adjacency matrix A where $A_{ij} = 1$ for $j \neq i$ when vertices v_i and v_j are connected, zero otherwise, and $A_{ii} = 0$. The coupling function $H : \mathbf{R} \to \mathbf{R}$ is differentiable and must satisfy $H'(0) > 0$. Examples include $H(x) = \sin(x)$ for the stochastic Kuramoto model and $H(x) = \sin(x-\zeta)$ for the stochastic Kuramoto-Sakaguchi model [26]. For $i = 1,\dots,N$, the ω_i are constants modelling the natural frequency of the i'th oscillator at vertex v_i. We consider identical oscillators in this paper for which, through a shift to the centre of mass, the ω_i may be set to zero. However, in analytical considerations we take the natural frequencies as non-zero to derive more general expressions, and only set them to zero in the final step. In numerical simulations they will be set to zero.The x_i is the initial position of the i'th oscillator at time $t = 0$. The quantity $K > 0$ is a real-valued coupling constant. We will absorb N into K from this point onwards and use the rescaled coupling constant $\kappa := \frac{K}{N}$.

The stochastic perturbations in the dynamical system are given by a N-dimensional Lévy process $L := (L_1(t),\dots,L_N(t))_{t\geq 0}$ where the i'th component perturbs the i'th vertex v_i. The class of Lévy processes can be characterised as follows (e.g., see [27]). If $L := (L(t))_{t\geq 0}$, $L(0) = 0$, is a Lévy process defined on the probability space $(\Omega,\mathcal{F},\mathbf{P})$, then the characteristic function of L has the Lévy-Khintchine representation $\Phi(k) := \mathbf{E}[e^{ikL_t}] = e^{t\Psi(k)}$ with characteristic exponent

$$\Psi(k) := ik^T\gamma - \frac{1}{2}k^T Q k + \int_{\mathbf{R}} (e^{ix^Tk} - 1 - ix^T k\,\mathbf{1}_\circ(x))\,\nu(\mathrm{d}x), \tag{2}$$

for $k \in \mathbf{R}^N$ and $x^T y = \sum_{i=1}^N x_i y_i$ with $x, y \in \mathbf{R}^N$. Here, $\mathbf{E}$ denotes the expectation operator, defined as $\mathbf{E}[X] := \int_\Omega X\,d\mathbf{P}$, for $X : \Omega \to \mathbf{R}^N$ a random variable on the probability space $(\Omega,\mathcal{F},\mathbf{P})$ and $\mathbf{1}_\circ$ is the indicator function such that $\mathbf{1}_\circ(x) = 1$ if $\|x\| \leq 1$ and 0 otherwise. The $N\times N$ matrix Q is symmetric nonnegative-definite, $\gamma \in \mathbf{R}^N$, and the measure ν satisfies $\nu(\{0\}) = 0$ and $\int_{\mathbf{R}^N} \min(\|x\|^2, 1)\,\nu(\mathrm{d}x) < \infty$. Equivalently, we say L has the canonical triplet (γ, Q, ν) where ν is called the Lévy measure. When $N = 1$ and $(a,b] \subset \mathbf{R}$, then the Lévy measure has the interpretation that $\nu((a,b])$ is the rate at which the process takes jumps of size between a and b per unit of time. The class of Lévy process is broad and includes, for example in the $N = 1$ case, processes such as the Brownian motion with drift $(\gamma,\sigma^2,0)$ and the Poisson process of rate λ with canonical triple $(0,0,\lambda\delta_1)$ where δ_1 is the point mass at 1. We give a more explicit example in Section 3.5.

We follow the customary approach that the initial positions are taken to be randomly distributed according to various probability distributions. In our simulations, we take the frequencies to be zero and the initial positions uniformly distributed over $(-\pi,\pi]$ and independent between themselves. We take the network topology to be stochastic and independent from all other sources of randomness. The

frequencies, the initial positions, and the network topology are all randomly sampled at time $t = 0$ and then remain fixed for $t > 0$. This means that for $t > 0$, the only source of randomness in the system is the Lévy process L. The graph $\mathcal{G}$ will be randomly sampled from two distributions: the classic ER and the BA scale-free. The former is generated by considering N vertices and M edges so that any two vertices are connected with uniform probability $N/2M$. The latter is based on preferential attachment whereby starting from m_0 connected vertices, new vertices are introduced connecting to $m \leq m_0$ vertices with a probability proportional to the degree of the existing vertices, which is then iterated. This procedure generates a power law degree distribution d^{-3}, where $d_i := \sum_{j\neq i} A_{ij}$ is the degree of a given node i. Such a distribution for d leads to a 'hub' or core of the network in contrast to the more heterogeneous structure of the ER graph. We recall that for networks with degree spectra $d^{-\varepsilon}$ with exponent $2 < \varepsilon < 3$ there is no synchronisation for the Kuramoto model for any size network [21].

3. The dynamics close to synchronisation

3.1. Solution near synchronisation

Close to synchronisation, that is $\theta_i \approx \theta_j$ for all $v_i, v_j \in V$, we are able to analytically approximate the behaviour of our proposed dynamical system. We recall that the order parameter $r(t)$ is given by

$$r(t) := \frac{1}{N}\left|\sum_j e^{i\theta_j(t)}\right|. \tag{3}$$

This parameter enables measurement of the collective system behaviour. For example, for coupling K greater than some critical value K_c and zero noise ($L_i(t) \equiv 0$ for all $1 \leq i \leq N$ and $t \geq 0$), the order parameter $r(t)$ reaches a plateau close to 1 as $t \to \infty$ when the phases at all the vertices synchronise. The critical coupling K_c is usually defined as value at which the order parameter, when averaged over many instances and at $t \to \infty$ (or, alternately, time-averaged), first deviates from zero after accounting for finite-size scaling. This value marks the onset of synchronisation. Note that a critical value of K occurs even for the system of identical oscillators in the absence of noise. For example, even such a simple system may have frequency synchronised (in contrast to phase synchronised) fixed points that are unstable [28]. Naturally, the addition of noise further impedes the achievement of $r = 1$.

We consider Eq.(1) and recall that we posed H to be smooth function satisfying $H'(0) > 0$. This holds for the Kuramoto case $H(x) = \sin(x)$ and the Kuramoto-Sakaguchi case $H(x) = \sin(x - \zeta)$ when $\zeta \in (-\frac{\pi}{2}, \frac{\pi}{2})$. We take a first-order approximation of H around zero $H(x) \approx H(0) + xH'(0)$ to obtain a SDE for the linearised dynamics $\widetilde{\theta}_i(t)$ of each $\theta_i(t)$ given by

$$\mathrm{d}\widetilde{\theta}_i(t) = \left[\widetilde{\omega}_i - \kappa H'(0)\sum_{j=1}^{N}\mathcal{L}_{ij}\widetilde{\theta}_j(t)\right]\mathrm{d}t + \mathrm{d}L_i(t), \tag{4}$$

with $\widetilde{\omega}_i := \omega_i + \kappa H(0)d_i$ and $d_i = \sum_{j=1}^{N} A_{ij}$ is the degree of vertex v_i. The $N \times N$ matrix $\mathcal{L}$ is the graph Laplacian (e.g., [29])

$$\mathcal{L}_{ij} := D_{ij} - A_{ij}, \tag{5}$$

where D has all elements zero except for the diagonal whose elements are given by the degrees d_i of the vertices. As the process $\widetilde{\theta}$ is now linear, by defining $B := \mathrm{diag}_N(\kappa H'(0))\mathcal{L}$ and posing the system in terms of the moving frame of reference as $\widetilde{\theta}^x(t) := \widetilde{\omega}t + X^x(t)$, then the dynamics for $X^x(t) \in \mathbf{R}^n$ can be written compactly in vector-matrix form as the Lévy Ornstein-Uhlenbeck (LOU) equation

$$\begin{cases} \mathrm{d}X^x(t) = -BX^x(t)\mathrm{d}t + \mathrm{d}L(t), & t > 0, \\ X^x(0) = x \in \mathbf{R}^N, \end{cases} \tag{6}$$

where $L(t) := (L_1(t), \ldots, L_N(t))^T$ and $x := (x_1, \ldots, x_N)^T$ is the initial position of the oscillator system. We assume the N-dimensional Lévy process $L := (L(t))_{t\geq 0}$ has characteristic exponent Ψ given by Eq.(2). The solution for $(\widetilde{\theta}^x(t))_{t\geq 0}$ follows by solving Eq.(6) and is given by a shifted form of the Lévy Ornstein-Uhlenbeck process

$$\widetilde{\theta}^x(t) = \widetilde{\omega}t + e^{-tB}x + \int_0^t e^{-(t-s)B}\,dL(s), \quad t \in \mathbf{R}_+. \tag{7}$$

3.2. Transition probabilities

For any continuous function $\varphi : \mathbf{R}^d \to \mathbf{R}$ vanishing at $|x| \to \infty$, the semigroup $(R_t)_{t\geq 0}$ is given by

$$\begin{aligned} R_t\varphi(x) := \mathbf{E}\varphi(\widetilde{\theta}^x(t)) &= \int_{\mathbf{R}^N} \varphi(\widetilde{\omega}t + y)\eta_t(x, \mathrm{d}y) \\ &= \int_{\mathbf{R}^N} \varphi(\widetilde{\omega}t + e^{-tB}x + y)\eta_t(\mathrm{d}y), \end{aligned}$$

where $\eta_t(x, \cdot)$ is the transition probability of $\widetilde{\theta}^x(t)$ and for convenience we have written $\eta_t(\cdot) := \eta_t(0, \cdot)$.

By standard results on LOU processes [27] and since B is symmetric, the characteristic function of the time-dependent process (7) has the explicit representation for any $z \in \mathbf{R}^n$,

$$\widehat{\eta}_t(x,z) := \mathbf{E}[e^{i\theta^x(t)^T z}] = \exp\left(\widetilde{\omega} t z + i x^T e^{-tB} z + \int_0^t \Psi(e^{-sB} z)\,\mathrm{d}s\right),$$

where Ψ is the characteristic exponent of L.

3.3. Invariant measure

When $\widetilde{\omega} = 0$ (which holds when entering the rotating frame $\theta(t) \mapsto \theta(t) + \mathbf{E}[\widetilde{\omega}]t$ and by the results of [30], the process (7) has an invariant measure if

$$\int_{|z|>1} \log|z|\,\nu(\mathrm{d}z) < \infty. \tag{8}$$

If (8) holds, then it follows that when $t \to \infty$ the characteristic function of the invariant measure η_∞ for $z \in \mathbf{R}^n$ is

$$\widehat{\eta}_\infty(z) = \exp\left(\int_0^\infty \Psi(e^{-sB} z)\,\mathrm{d}s\right), \tag{9}$$

where Ψ is the characteristic exponent of L.

3.4. Distilling the collective dynamics

Using the singular value decomposition we see the role that the positivity of the spectrum of the graph Laplacian [31] plays in the stability of the deterministic limit of the system. Some well-known analytic results are given in [31] and we give in Fig.1 the histogram of eigenvalues for the BA and ER cases that we use in our numerical study. Beyond such perturbative arguments (see also [32, 33]), there is numerical evidence for the Kuramoto model [34] that the Laplacian remains an effective means of distilling the collective dynamics even before the onset of phase synchronisation.

The network $\mathcal{G}$ is connected and undirected so all the N eigenvalues of $\mathcal{L}$ are real and can be ordered $0 = \ell_0 \le \cdots \le \ell_{N-1}$ with associated eigenvectors $u^{(0)} \ldots u^{(N-1)}$ of $\mathcal{L}$. Even though there are as many eigenvalues as nodes of the network, we use the label $m = 0, \ldots, N-1$ for eigenvalues to distinguish labels $i = 1, \ldots, N$ for vertices of the network. We normalise the eigenvectors $\{u^{(m)}\}_{m=0}^{N-1}$ so they form an orthonormal basis for $\mathbf{R}^N$. The eigenvector associated with $\ell_0 = 0$ is $u^{(0)} = \mathbf{1}$. Following from the spectral decomposition of $\mathcal{L}$,

$$B = \sum_{m=1}^{N} \kappa H'(0) \ell_m u^{(m)} u^{(m)T}. \tag{10}$$

The process projected on the m'th eigenvector is given by $X_m(t) := u^{(m)T} \widetilde{\theta}^x(t)$. Later we use the projection of the vector of native frequencies on Laplacian eigenvectors which we represent by

$$\omega^{(m)} := \sum_{i=1}^{N} \omega_i u_i^{(m)}. \tag{11}$$

A key property of Laplacian eigenvectors that we will use below is that the sum over the components of any individual normal ($m \neq 0$) eigenvector is zero,

$$\sum_{i=1}^{N} u^{(m)} = 0, \tag{12}$$

a consequence of the orthonormality to the zero eigenvector and that the latter has components all identical to unity.

3.5. The influence of tail behaviour on synchronisation

As our aim is to understand how the tail behaviour of the Lévy process L influences synchronisation in the dynamical system, we focus on a particular case of Lévy process: the tempered stable process. This process provides analytical control on the rate of decay of its tail through a parameter λ which will allow us to study how this affects synchronisation behaviour.

For simplicity, the processes considered in this section will be of jump type, i.e., $Q = 0$, with the Lévy measure of product form $\nu = \prod_{j=1}^{N} \nu_j$ with ν_j describing the jumps that apply to the j'th oscillator θ_j. This allows us to consider the process L componentwise through its j'th component L_j and decomposes the characteristic exponent as $\Psi(k) = \sum_{j=1}^{N} \Psi_j(k_j)$ with $k = (k_1, \ldots, k_N)^T \in \mathbf{R}^N$.

The tempered stable process is best understood by starting with the definition of a stable process whose transition probabilities are also known as *fractional diffusion* [35]. The j'th component L_j of the Lévy process L is called a (totally positively skewed) *stable process* if the characteristic exponent $\Psi_j(k)$ satisfies for $k \in \mathbf{R}$ the explicit expression

$$\Psi_j(k) = a\Gamma(-\alpha)\cos\Big(\frac{\pi\alpha}{2}\Big)|k|^\alpha\Big(1 - i\tan\Big(\frac{\pi\alpha}{2}\Big)\mathrm{sgn}(k)\Big), \tag{13}$$

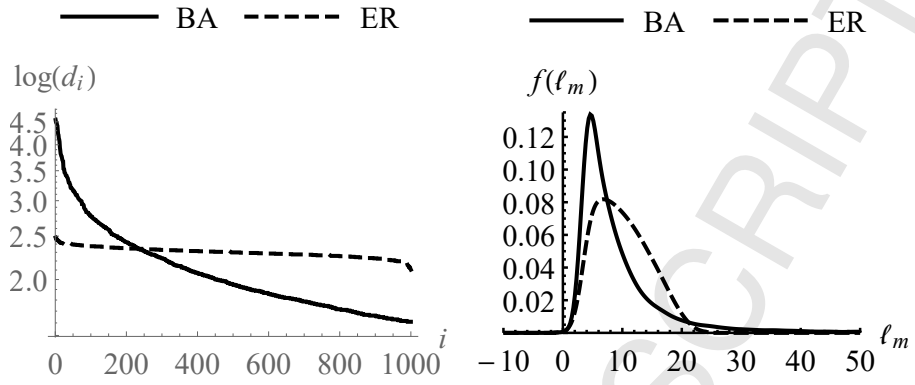

Figure 1: Degree distributions (left) and frequency distribution f of Laplacian eigenvalues ℓ_m (right) for the Barabasi-Alberts 'scale free' and Erdős-Rényi random graphs with 1,000 vertices used in our numerical study; the spectra are averaged over 30 instances of graphs from each class.

where $a > 0$ and $\alpha \in (0,1) \cup (1,2)$. That is, we exclude the Cauchy process ($\alpha = 1$). The expression given in Eq.(13) is obtained by considering $\int_0^\infty (e^{ikx} - 1)\frac{a}{x^{\alpha+1}}\,\mathrm{d}x$ for $\alpha \in (0,1)$ and $\int_0^\infty (e^{ikx} - 1 - ikx)\frac{a}{x^{\alpha+1}}\,\mathrm{d}x$ for $\alpha \in (1,2)$. These two representations highlight that the Lévy measure has the form $\nu_j(\mathrm{d}x) = a/x^{\alpha+1}\,\mathrm{d}x$. Tempering the Lévy measure of the stable process by introducing an exponential decay leads to L becoming a (totally positively skewed) *tempered stable process*. In other words, the characteristic exponent Ψ_j for the j'th component L_j of L is given by

$$\Psi_j(k) = \begin{cases} \displaystyle\int_0^\infty (e^{ikx} - 1)\frac{a e^{-\lambda x}}{x^{\alpha+1}}\,\mathrm{d}x, & \alpha \in (0,1), \\ \displaystyle\int_0^\infty (e^{ikx} - 1 - ikx)\frac{a e^{-\lambda x}}{x^{\alpha+1}}\,\mathrm{d}x, & \alpha \in (1,2), \end{cases}$$

with $a > 0$, $\alpha \in (0,1) \cup (1,2)$, and $\lambda > 0$. Let S_t be the stable process at time t, then alternatively, this stable process admits a density at any time t but cannot be written down as a closed-form formula [27]. Without loss of generality, we take $t = 1$. Then the tempered stable density $f_{\mathrm{TS}(\alpha,a,\lambda)}$ can be obtained by tempering the stable density $f_{\mathrm{S}(\alpha,a)}$ of S_1 as

$$\begin{aligned} \frac{e^{-\lambda x}}{\mathbf{E}[e^{-\lambda S_1}]} f_{\mathrm{S}(\alpha,a)}(x) &= e^{-\lambda x - a\Gamma(-\alpha)\lambda^\alpha} f_{\mathrm{S}(\alpha,a)}(x) \\ &=: f_{\mathrm{TS}(\alpha,a,\lambda)}(x), \end{aligned}$$

which leads to

$$f_{\mathrm{TS}(\alpha,a,\lambda)}(x) = e^{-\lambda x - a(1-\alpha)\Gamma(-\alpha)\lambda^\alpha} f_{\mathrm{S}(\alpha,a)}(x + \Gamma(1-\alpha)a\lambda^{\alpha-1});$$

see [36] for more details. A two-sided tempered stable process $(L_t^\beta)_{t\geq 0}$ of index α can be obtained from two independent positively skewed tempered stable processes $(T_t)_{t\geq 0}$ and $(\widetilde{T}_t)_{t\geq 0}$ as $L_t^\beta := (1+\beta)T_t - (1-\beta)\widetilde{T}_t$ with $-1 \leq \beta \leq 1$. Then performing the integrals in Eq. (14) gives the explicit form for the characteristic exponent $\Psi_j(k)$ for the two-sided case as

$$\begin{aligned} \Psi_j(k) = -a\big[&(1+\beta)(\lambda + ik)^\alpha + (1-\beta)(\lambda - ik)^\alpha \\ &- 2\lambda^\alpha - 2ik\alpha\beta\lambda^{\alpha-1}\Theta(\alpha-1)\big] \end{aligned} \quad (14)$$

with $\Theta(x)$ the heaviside step function: $\Theta(x) := 1$ for $x > 0$ and zero otherwise; see [37].

If S_t is a stable process at time t, then the probability distribution of S_t only has moment m if $m < \alpha$ which is restrictive in practice as $\alpha \in (0,1) \cup (1,2)$. However, if L_t is a tempered stable process then irrespective of the value of α the first moment of L_t, without loss of generality at $t = 1$ and $N = 1$, exists and is given by

$$\mathbf{E}[L_1] = \frac{1}{i}\Phi'(0) = \begin{cases} a b^{\alpha-1}\Gamma(1-\alpha), & 0 < \alpha < 1, \\ 0, & 1 < \alpha < 2, \end{cases} \quad (15)$$

and the second moment is

$$\begin{aligned} \mathbf{E}[L_1^2] &= \frac{1}{i^2}\Phi''(0) \\ &= \begin{cases} a b^{\alpha-2}(a b^\alpha \Gamma(1-\alpha)^2 + \Gamma(2-\alpha)), & 0 < \alpha < 1, \\ a b^{\alpha-2}\Gamma(2-\alpha), & 1 < \alpha < 2, \end{cases} \end{aligned}$$

We take the parametrisation

$$a := -\frac{1}{2}\sigma^2 \frac{1}{\Gamma(-\alpha)\cos(\pi\alpha/2)}, \quad \tilde{a} := a/\Gamma(-\alpha) \tag{16}$$

so that we have $\lim_{\alpha\to 2}\mathbf{E}[L_1^2] = \sigma^2$. In other words, $\Psi_i(k) \to -\frac{1}{2}\sigma^2 k^2$ as $\alpha \to 2$ to recover the Brownian motion in the limit. In other words, when $\alpha = 2$, L is a N-dimensional Brownian motion with canonical triple $(0, Q, 0)$ with $Q = \mathrm{diag}(\sigma_1^2, \ldots, \sigma_N^2)$ and we choose $\sigma = \sigma_1 = \ldots = \sigma_N$. This parametrisation will be used in our study to show how the dynamics of the system change as α varies and converges to the classic 'diffusion' case when $\alpha = 2$ that other authors have studied [7, 6, 8, 15]. Further, notice that tempering has no effect on the decay of the tails in the Gaussian case ($\alpha = 2$).

For any continuous function $\varphi : \mathbf{R}^N \to \mathbf{R}$ vanishing at $|x| \to \infty$ the transition semigroup (P_t) of L is given by

$$P_t\varphi(x) = \mathbf{E}[\varphi(x + L(t))] = \int_{\mathbf{R}^N} \varphi(y) p_t(x, \mathrm{d}y), \tag{17}$$

where $p_t(x,\cdot)$ is the transition probability of L starting at x. In other words, $p_t(x, B) := \mathbf{P}\{x + L(t) \in B\}$ for $B \in \mathcal{B}(\mathbf{R}^N)$. Take $N = 1$ for simplicity, then as the (two-sided) tempered stable process has a density, we write $p_t(x, \mathrm{d}y) = \mathcal{U}(t, x-y)\mathrm{d}y$ in Eq.(17). The densities $\mathcal{U}(t,x)$ satisfy the *tempered space-fractional diffusion equation* given by

$$\partial_t \mathcal{U}(t,x) = (1-\beta)\tilde{a}\partial_x^{\alpha,\lambda}\mathcal{U}(t,x) + (1+\beta)\tilde{a}\partial_{-x}^{\alpha,\lambda}\mathcal{U}(t,x), \tag{18}$$

where $\partial_x^{\alpha,\lambda} := e^{-\lambda x}\,{}_{-\infty}D_x^\alpha e^{\lambda x}$ and $\partial_{-x}^{\alpha,\lambda} := e^{\lambda x}\,{}_xD_\infty^\alpha e^{-\lambda x}$ are the λ-tempered fractional derivatives of order α where the operators ${}_{-\infty}D_x^\alpha$ and ${}_xD_\infty^\alpha$ are the Riemann-Liouville derivatives; see [37].

Again assuming $N = 1$, it follows from the fact that

$$\int_{|x|>1} \log|x| \frac{a}{x^{1+a}} = \frac{1}{a}, \tag{19}$$

that the tempered stable process has an invariant measure when entering the rotating frame $\theta(t) \mapsto \theta(t) + \mathbf{E}[\tilde{\omega}]t$. Or, equivalently, we say that a steady-state density for the tempered stable space-fractional diffusion equation (18) exists.

We go over to the diffusion equation formulation of the linearised stochastic Kuramoto model, where we seek a time-dependent probability distribution of the Laplacian eigenvector projected phases, X_m, that is a product of densities for each m,

$$P(t, X) = \prod_{m=0}^{N-1} P_m(t, X_m).$$

For simplicity we take $\beta = -1$, then each marginal density satisfies the full tempered fractional Fokker-Planck equation [37]

$$\begin{aligned}\partial_t P_m(t, X_m) = {} & 2\tilde{a}\partial_{X_k}^{\alpha,\lambda} P_m(t, X_m) \\ & - \partial_{X_m}\left((\omega^{(m)} - \kappa\ell_m X_m)P_k(t, X_m)\right),\end{aligned} \tag{20}$$

which draws upon the tempered fractional derivative introduced in Eq.(18).

In this work we focus on the steady-state solutions of Eq.(20), $\partial_t P_m^s(t, X_m) = 0$, where the superscript 's' denotes steady-state. For example, taking $\alpha \to 2$ we obtain the steady-state density for the Gaussian case, found in [38]:

$$P_m^s(X_m) = \sqrt{\frac{\kappa\ell_m}{\sigma^2}}\, e^{-\frac{\kappa\ell_m}{\sigma^2}\left(X_m - \frac{\omega^{(m)}}{\kappa\ell_m}\right)^2}. \tag{21}$$

We observe here a Gaussian smearing about the deterministic solution $X_m^* = \frac{\omega^{(m)}}{\kappa\ell_m}$. With $\omega_i = 0$, as in our numerical simulations, the Gaussian is centred at $X = 0$. For small σ, correspondingly large κ, the Gaussian tail suppresses the probability that $X \neq 0$ prohibiting the system from 'escaping' the phase-synchronised solution.

While the untempered case ($\lambda = 0$) can be solved in closed form in terms of the Fox's H-functions [35], the steady state solution of Eq.(20) is best achieved by Fourier transformation. The tempered fractional derivative leads to the exponent of the characteristic function of the underlying distribution from Eq.(14), $\Psi = \ln\Phi_1(k|\alpha,\beta,\lambda) = \sigma^2\hat{\Psi}$, where we make the dependence on the noise constant σ explicit by this rescaling. Imposing the steady state condition $\partial_t P_m^s = 0$ in Eq.(20) and taking the Fourier transform gives the momentum space differential equation (see also [37, 9])

$$\kappa\ell_m k_m \frac{d}{dk_m}\tilde{P}_m^s = \left[\sigma^2\hat{\Psi}(k_m) - i\omega^{(m)}k_m\right]\tilde{P}_m^s, \tag{22}$$

where k_m is the conjugate to X_m. This is solved to give, including the correct normalisation,

$$\begin{aligned}P_m^s(X_m) = {} & \frac{1}{2\pi}\int_{-\infty}^{\infty} dk\, e^{ik_m(X_m - \frac{\omega^{(m)}}{\kappa\ell_m})} \\ & \times \exp\left[\frac{\sigma^2}{\kappa\ell_m}\int_0^{k_m} dk'\frac{\hat{\Psi}(k')}{k'}\right].\end{aligned} \tag{23}$$

Now setting the frequencies to zero the multi-dimensional steady-state probability density function is

$$P^s(\vec{X}) = \frac{1}{(2\pi)^{N-1}} \int_{-\infty}^{\infty} d^{N-1}k\, e^{ik^T X} \times \exp\left[\frac{\sigma^2}{\kappa \ell_m} \sum_{m=1}^{N-1} \int_0^{k_m} dk'_m \frac{\hat{\Psi}(k'_m)}{k'_m}\right] \quad (24)$$

Finally, we need to re-express the exponent $\hat{\Psi}$ of the characteristic function of the Laplacian projected process in terms of that for the original, namely of the process dL_i. To do this, first we recall the definition in terms of the Fourier transform for any given component:

$$\Phi(t)(k_m) := \int dL^{(m)} e^{ik_m L^{(m)}} p(t, L^{(m)}) \quad (25)$$

and substitute $p(t, L^{(m)})$ in Eq.(25) with its transformation on to the projected variables

$$p(t, L^{(m)}) = \int \prod_i^N dL_i \delta(L^{(m)} - \sum_j u_j^{(m)} L_j) p(t, L_i). \quad (26)$$

Interchanging the order of integration gives

$$\Phi(t)(k_m) = \int \prod_i^N dL_i \int dL^{(m)} \delta(L^{(m)} - \sum_j u_j^{(m)} L_j) \times e^{ik_m L^{(m)}} p(t, L_i). \quad (27)$$

We perform then the integral over $L^{(m)}$, implementing the delta function, to obtain

$$\Phi(t)(k_m) = \int \prod_i^N dL_i e^{ik_m \sum_j u_j^{(m)} L_j} p(t, L_i) = \int \prod_i^N dL_i e^{ik_m u_i^{(m)} L_i} p(t, L_i). \quad (28)$$

Each factor in this expression is a characteristic function for a corresponding component, but with the process L_i replaced by $u_i^{(m)} L_i$, so that the characteristic exponent for each i is just Ψ with a rescaled momentum k. Thus overall the new exponent is the sum of the individual ones but with rescaled arguments:

$$\Phi(t)(k_m) = \exp\left[-t\, a \sum_i \Psi(k_m u_i^{(m)})\right] \quad (29)$$

so that in Eq.(23) we insert

$$\hat{\Psi}(k) = a\left[(1+\beta)\sum_i (\lambda + ik u_i^{(m)})^\alpha + (1-\beta)\sum_i (\lambda - ik u_i^{(m)})^\alpha - 2N\lambda^\alpha\right] \quad (30)$$

using the vanishing of the sum over eigenvector components, Eq.(12), in the Θ term of Eq.(14).

Unfortunately because of the λ dependence in Eq.(30) it is not possible to cleanly separate out the role of the Laplacian eigenvectors other than that they individually re-weight the 'momentum' in the characteristic exponent. This is in contrast to the stable case where such a separation is possible with dependence shown in Fig.10 of our previous work [9].

With the σ^2 dependence, we see in this result again that for vanishing frequencies again the diffusion constant and coupling combine into the universal coupling $g = \sigma/\sqrt{\kappa}$. Further analytic progress is only possible for $\lambda = 0$, as shown in our earlier work [9]. Thus two integrals must be computed numerically for the tempered case. For smaller values of α, because tails become fat, the Fourier transform can be become numerically intensive and the integrand as a function of k is well-behaved. We compute Fourier integrals by approximating as a discrete Fourier transform with periodic boundary conditions for the real part (and associated zero mode) and antisymmetric boundary conditions for the imaginary part. For small α we take a discrete momentum step of $\Delta k = 0.1$ and sum up to 5×10^5 points.

In the following we illustrate particular cases of this solution for $\sigma = 3, \kappa = 1$ and $\lambda = 0.01, 0.2, 1$, to give results comparable to the stable cases in [9]. The critical insight we seek to gain from the shape of these distributions is where their support lies in relation to the region $-1 < X_m < 1$ describing, based on the decomposition of the deterministic system, the basin of attraction for phase synchronisation. To gain a picture of the multi-dimensional solution to the Fokker-Planck $P^s(\vec{X})$ we consider a subset of modes m that correspond to key regions in the Laplacian spectra for the two types of networks as shown in Fig.1. To that end, and as in [9], we choose seven values m as shown in Table 1 to visualise, on the one hand, the higher multiplicity of modes with eigenvalue of order one in the BA case ($m = 399$ is still at value 5.8 for BA, but for ER it is 8.2), and, on the other hand, the long tail of eigenvalues for the BA case (the last mode $m = 999$ has eigenvalue 122.8 whereas ER is

23.8). Each value of m identifies a direction or dimension in the multi-dimensional space of the probability distribution. Furthermore, for the eigenvectors in Eq.(30) we use the average $\langle u_i^{(m)} \rangle$ over an ensemble of 30 graphs for each of the BA and ER types.

These plots are indeed visually indistinguishable from those in Fig.8 of [9] for purely stable noise close to the Gaussian limit; tempering effects are negligible here. We include these plots here in order to reiterate the mechanism given in our previous work [9] for the cross-over between BA and ER graphs near the Gaussian limit for the order parameter dependence as a function of noise strength σ. In this case we examine the behaviour for small $\lambda = 0.001$. We plot in Fig.2 the solutions to the Fokker-Planck equation for various σ at $\alpha = 1.99, \lambda = 0.001$, in the top row for BA networks, and the bottom row for ER networks. Different modes m are superimposed on the same curve for a given value of σ, α and λ so that the shape of the distribution in different dimensions may be visualised.

We observe at low $\sigma = 0.5$ the narrowness of the Fokker-Planck distributions around the origin, consistent with the Kuramoto system with vanishing natural frequencies showing high synchronisation when subject to low noise strength. At higher noise strength, $\sigma = 1-2$ (second plots from the left of Fig.2 top and bottom) we see broadening of the distributions, however for the BA case the tails remain still somewhat suppressed beyond $X = \pm 1$ for small m. Iin comparison the ER case shows all modes broadening. At $\sigma = 3$ (right-most plots in Fig.2 top and bottom), the ER case is very broad including its highest modes while the BA case has its highest modes still quite narrow. Overall, with increasing σ the ER graph is the first to show directions where its distribution develops tails outside the basin of attraction in more directions than for the BA graph. As explained in [9], these effects are a consequence of the tail of its Laplacian spectrum driving the Gaussian broadening of the distribution. Thus, the BA graph loses synchrony more 'gracefully' than the ER graph.

Given the result in Fig.2 that densities narrow as one goes higher in the Laplacian spectrum, we now study tempering on the lowest Laplacian mode $m = 1$, the broadest and therefore the most prone to escape the basin of attraction under broadening of the Fokker-Planck distribution. In Fig.3 we show results for a range of tempering, $\lambda = 0.01$ (top), $\lambda = 0.2$ (middle) and $\lambda = 1$ (bottom). On the left we show the results for the tempered fractional Fokker-Planck densities for the BA graph case and on the right for the ER case. We compare for fixed σ the densities for decreasing α below $\alpha = 1.5$. On the top row, with very small tempering, we observe a result similar to that already shown in Fig.2: as α decreases the densities broaden and tails of Fokker-Planck densities become heavier. Again, the ER densities (right) are slightly broader than those for the BA graph. On the second row, with 'slight' tempering at $\lambda = 0.2$, we see the expected effect for $\alpha \in (0.5, 1.5)$ the broadening of the distributions as α decreases. However, with further decrease below $\alpha = 0.5$ the distributions *narrow again*; the ER case is again broader than BA but shows the same effect. Finally, with $\lambda = 1$ the tendency of the top row is reversed: densities narrow with decreasing α across the entire range $\alpha \in (0, 2)$. In other words, synchronisation would be expected to improve with decreasing α in the presence of tempering because of an increased probability of remaining in the basin of attraction.

Thus the analytic solution based on linearising around the phase synchronised fixed point predicts an improvement in synchronisation at fixed σ and λ for decreasing α below $\alpha = 1$. We now examine the behaviour of simulations to test this prediction.

4. Dynamics away from synchronisation

In this section we study the system numerically away from synchronisation in the tempered stable case. For identical frequencies in the Kuramoto model the noise strength and coupling can be brought together into a single coupling constant $g = \sigma/\sqrt{\kappa}$, for both Brownian [7] and stable Lévy noise [9]. We extend the argument here to tempered noise. First, we go to a frame of reference where $\omega_i = 0$, so that the equation of motion Eq.(1) may be recast with time rescaled as $\tau = \kappa t$. The noise then becomes $(1/\kappa)L_i(\tau/\kappa)$, where for each i we use the same $\alpha, a, \beta, \mu, \lambda$. Using the dependence of the characteristic function $\Phi_t(k)$ on time via the prefactor $t\,a$ in the exponential, Eq.(14), with $a \propto \sigma^2$ as in Eq.(16), we see that in the rescaled system this dependence is as $\tau\sigma^2/\kappa = \tau g^2$. For this reason, in the following simulations we fix the coupling to $\kappa = 1$ and vary the noise strength σ.

4.1. Simulation approach

In simulating the Kuramoto model subject to noise, we also generated 30 examples of graphs in each of the classes, BA and ER, using the *RandomGraph* function of Wolfram's Mathematica 10. In

Table 1: Laplacian eigenvalue choices for Barabasi-Alberts and Erdős-Rényi graphs of $N = 1000$, $\bar{d} = 10$ and averaging over 30 instances

Graph	m=1	m=9	m=59	m=399	m=699	m=989	m=999
BA	2.88482	3.06324	3.53206	5.85223	9.74233	62.9679	122.802
ER	1.28646	2.5929	3.93219	8.19271	12.3496	20.456	23.8308
Colour	Black	Dark Grey	Grey	Blue	Purple	Brown	Red

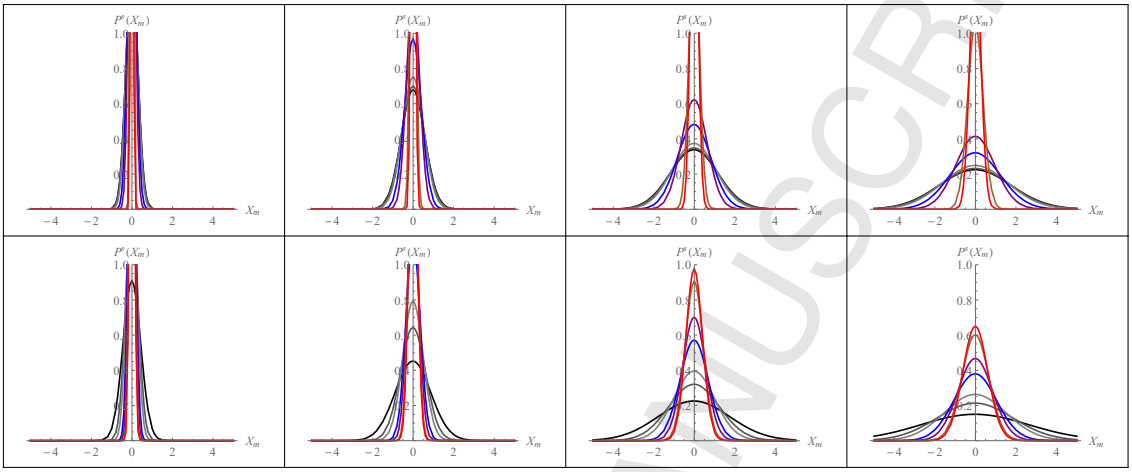

Figure 2: Solutions to the steady-state fractional Fokker-Planck equation for $\alpha = 1.99, \lambda = 0.001$ and different eigenvalues: top row Scale Free, bottom row Erdős-Renyi, from the left $\sigma = 0.5, 1, 2, 3$, with eigenmodes $m = 1$ in black, $m = 9$ in dark grey, $m = 59$ in light grey, $m = 399$ in blue, $m = 699$ in purple, $m = 989$ in brown, and $m = 999$ in red.

Fig.1 we present for ER and BA graphs of 1000 vertices and average degree $\bar{d} = 10$ the distribution of degrees d_i and the spectrum of the graph Laplacian

$$\mathcal{L}_{ij} := D_{ij} - A_{ij}, \tag{31}$$

where D has all elements zero except for the diagonal whose elements are given by the degrees of the vertices. This construct turns out to be useful for understanding the behaviour of the system close to synchrony. The eigenvalues shown in Fig.1 represent an average over 30 instances of the graph of each class for every discrete mode number labelled by m; in our convention $m = 0, \ldots, 999$, where $m = 0$ corresponds to an exactly vanishing eigenvalue.

To simulate the Kuramoto dynamics with Lévy noise, we use an Euler scheme on the N-dimensional stochastic differential equation given by (1). We choose the number of mesh points $M > 0$ so that the time increment $\Delta t := T/M$, then the true N-dimensional dynamics $\theta(t) := (\theta_i(t))_{i=1}^N$ are approximated by $\theta^M(t) := (\theta_i^M(t))_{i=1}^N$ obtained as follows. We start by sampling the initial values $\theta_i^M(0) = x_i$ from the uniform distribution on the interval $[-\pi, \pi)$ and then simulate each N-dimensional path $t \mapsto \theta^M(t)$ at the time points $\Delta t, 2\Delta t, \ldots, M\Delta t = T$ through a Euler scheme. Denoting $\theta_i^M[s] := \theta_i^M(s\Delta t)$, the scheme is given componentwise for $1 \le i \le n$ by

$$\theta_i^M[s+1] = \theta_i^M[s] + A_{ij} \sin(\theta_i^M[s] - \theta_j^M[s])\Delta t + \xi_i[s] \tag{32}$$

for integers $0 \le s < M-1$ and $0 \le i, j \le N$ with $i \ne j$. The random variables $\xi_i[s]$ are distributed like an increment of the Lévy process $dL(t) \sim L_{\Delta t}$ for $1 \le i \le N$ and $0 \le r \le M-1$. The computational difficulty lies in the simulation of the random variables $\xi_i[s]$ with distribution $L_{\Delta t}$.

To simulate $L_{\Delta t}$ in the tempered stable case requires two different algorithms: one for the case $0 < \alpha < 1$ and another for the case $1 < \alpha < 2$. We follow [39, 36] whereby for the case $0 < \alpha < 1$ we use an acceptance-rejection method that simulates the exact distribution. Unfortunately, for the case $1 < \alpha < 2$, no exact simulation methods are known and one must resort to an approximation; see [36] and the references therein. We use the acceptance-rejection algorithm that approximately simulates the distribution but depends on a parameter c. The parameter c truncates the real line $\mathbf{R}$ to the domain where the exponential tempering e^{-bz} is performed. In [39] it is shown that as $c \to \infty$ the probability density of

the sampled distribution converges in an $L^1(\mathbf{R})$-sense to the density of the true tempered stable distribution that we would like to draw samples from. Unfortunately, as c increases, the computational effort required by the algorithm increases as well. Therefore it is important to choose a finite c so that these concerns are balanced. As we are interested in understanding the behaviour of the Kuramoto model under a wide range of parameter choices, we resorted to the following approach to numerically find a good c given a, b and α.

Let $Q(p)$, $0 < p < 1$, be the quantile function of the tempered stable distribution $\mathrm{TS}(\alpha, a, \lambda)$, i.e., if F is the distribution function of $\mathrm{TS}(\alpha, a, \lambda)$ then $Q(p) := \inf\{x \in \mathbf{R} : p \le F(x)\}$. We can obtain the distribution function F through numerical Fourier inversion of Φ using a trapezoidal quadrature rule to approximate the integral

$$F(x) = \frac{2}{\pi}\int_0^\infty \frac{\sin(z\,x)}{z}\Re\Phi(z)\,dz,$$

where $\Re(x+iy) := x$ for $x, y \in \mathbf{R}$. Given a mesh size of h, the integral is approximated as

$$F(x) = \frac{h\,x}{\pi} + \frac{2}{\pi}\sum_{j=1}^{N}\frac{\sin(h\,j\,x)}{j}\Re\Phi(h\,j) - \varepsilon_h - \varepsilon_N \quad (33)$$

where ε_h is the discretization error associated with the choice of mesh size h and ε_N is the truncation error caused by taking $N < \infty$. To approximate $F(x)$ with good accuracy we set $h = 2\pi/(x + |m_1| + q|\sqrt{m_2 - m_1^2}|)$ where $m_1 = \mathbf{E}[T_1]$ and $m_2 = \mathbf{E}[T_1^2]$ are obtained explicitly through closed-form formulas and $q \in \mathbf{N}$ is chosen sufficiently large (e.g., $q = 5$). The upper bound of the summation is chosen to satisfy $|\Phi(hN)|/N < \pi\varepsilon/2$ where ε is the desired truncation error (which we set to the smallest ε such that $1 + \varepsilon \neq 1$ on our machine). Thus, given our numerical approximation $F^{h,N}$ of the distribution function F we apply a root finding procedure to identify the approximate quantile function $Q^{h,N}(p)$ of $F^{h,N}$ which usually converges in three to four iterations. Finally, for a given choice of α, a, b we choose c such that $c = -Q^{h,N}(p) - \Delta t\, a\Gamma(1-\alpha)a\,b^{\alpha-1}$ with $p = 0.05$.

In presenting results of simulations we show a quantile plot, otherwise known as a Q-Q plot, of the tempered stable distribution $\mathrm{TS}(\alpha, a, \lambda)$ against a normal distribution. That is if F is the cumulative distribution function (CDF) of $\mathrm{TS}(\alpha, a, \lambda)$, G the CDF of a standard normal distribution, and Q_F and Q_G are the associated quantile functions, the Q-Q plot draws the q-th quantile of F against the q-th quantile of G for a range of values of q. Thus, the Q-Q plot is a parametric curve ranging over $q \in [0,1]$ with values in the real plane $\mathbf{R}^2$. We also follow the standard convention to draw a (dashed) line through the points $(Q_G(0.25), Q_F(0.25))$ and $(Q_G(0.75), Q_F(0.75))$.

4.2. Simulation results

To compare directly with the results of [7] and our previous work [9], we consider ER and BA graphs of size $N = 1000$ and average degree $\bar{d} = 10$. We compute the order parameter as a function of time averaged over 128 paths (varying initial conditions and noise instance) for each time step and over 30 graphs, either BA or ER as specified. After checking that steady-state has been reached we extract the value of the order parameter at $t = 60$ as representative of r_∞. In Fig.4 we show the resulting values of r_∞ against σ for similar ranges of α and λ as used for the Fokker-Planck solutions, comparing ER and BA graphs.

Examining any one of the curves shows that the basic cross-over between BA and ER curves seen from the stable case [9] is ubiquitous. We see that for the stable noise case our results from [9] reproduced: for increasing σ the order parameter drops off sharply as a consequence of increasing probability of noise destroying the synchronisation; as α increases the range of σ over which the the order parameter remains close to unity also increases; and the loss of synchronisation of the BA graph is more graceful than the ER case. Next, for $\lambda = 0.1$ we clearly see the above behaviour is reversed: increasing $\alpha \in (0,1)$ diminishes the range in σ over which synchronisation is maintained. For increasing $\alpha \in (1,2)$ there is minimal change in the range of σ over which synchronisation is high. A slight increasing in λ to 0.2 further enhances this effect. Finally, at $\lambda = 1$ the range of σ giving high synchronisation decreases monotonically with increasing α, with the most dramatic changes in the range $\alpha \in (0,1)$.

These results confirm the insight based on the analytical results using linearisation around the phase synchronised fixed point. Moreover, they generalise this behaviour for regimes far from perfect phase synchrony: even for values $r \approx 0.5$, for which linearisation no longer applies, at fixed α and σ increased tempering improves the synchronisation.

4.3. Mechanism for improved synchronisation: pathwise dynamics

An intuitive picture to understand this improvement in synchronisation for decreasing α under tem-

pering follows from the basic shape of the underlying probability density for the continuous time random walk. In the stable noise case, as α decreases more mass from the centre of the density, where it finds its support, is pushed out to the tails leading to the power-law asymptotic behaviour. For $\alpha < 1$ this becomes so extreme that densities narrow around the mode of the distribution forming a cusp, with very long tails; essentially the noise favours either very small or very large values and excludes 'intermediate' scales. Tempering now imposes a smooth cutoff at asymptotic values so that for $\alpha < 1$ in particular, the distribution only favours very small values for the choice of the random jump. In the context of synchronisation such a profile for the jumps means that for fixed coupling, the size of additive jumps on oscillator motions decreases for decreasing α under tempering.

This mechanism leads us to anticipate otherwise counter-intuitive behaviour away from the pure synchronised regime. In [9] we observed in simulations of individual paths of oscillator dynamics an *induced drift* under skewed stable noise in spite of the frequencies being equal, a drift not completely explained by the skew of the noise distribution. Specifically, for $\alpha > 1$ the induced drift was in the *opposite* direction to the skew and for $\alpha < 1$ in the same direction as the skew. We recall that the skew determines the degree of one-sidedness of the heavy tail (maximal in our case with $\beta = 1$) and that for $\alpha < 1$ the stable distribution ceases to have even a finite first moment. Therefore, for $\alpha > 1$ the mode of the skewed stable distribution is in the opposite direction to the skew such that a zero mean is fulfilled: the mass around the mode 'balances' the heavy tail in the other direction, so to speak. For $\alpha < 1$ there is no such constraint, so mode and heavy tail lie in the same direction. For the oscillator system these properties mean that for $\alpha > 1$ there is a large cluster of oscillators that do not experience a large (positive) jump but the empirical mean of the average phase of this cluster will not vanish but follow the mode of the underlying noise. A negative drift, for positive skew, follows. For $\alpha < 1$ the mode reverses sign, so positive drift is induced.

Under tempering, the balance between the mass of the distribution and the tail is much more variable, with a finite non-zero mean for $\alpha < 1$. We expect then a much more subtle picture for the direction of the induced drift of the oscillators. In particular, because the heaviness of the tails is now suppressed, the corresponding shift of the mode is diminished so that the direction of the induced drift is not strictly determined by the skew.

We present here examples of individual oscillator paths for different values of α and λ to illustrate these different possibilities for the drift. These have been selected in a manner consistent with our previous work [9] where, after investigating a range of paths for various parameter settings, we identify that synchronisation begins to degrade at $\sigma = 2$. We then fix the random seed (fixing the network and oscillator initial conditions), vary across α and λ with $\beta = 1$ always. The examples here are for the ER graph, but qualitatively similar behaviours are seen for the BA topology. These results should be compared with those seen for the stable Lévy case in [9] where the same random seed was used.

Firstly, we mention that in the absence of noise and with $(\omega_i)_{i=1}^N = 0$, the $\theta_i(t)$ all converge to horizontal lines at zero; this represents *driftless* synchronisation. With $\alpha = 2$, Gaussian noise, paths also rapidly converge to a single horizontal trajectory but with small jitters around this line. Next, from Fig.3 in [9] we know for $\lambda = 0$ and $\alpha = 1.95$ that larger jumps appear amongst the jitters over the still horizontal trajectories that are 2π apart describing oscillators that have suffered jumps out of the synchronised cluster but that return after wrapping around the circle; as shown there the motion is still driftless.

In Fig.5 we show now in the left hand panel the result for selected $\theta_i(t)$ for tempered noise, $\lambda = 0.2$ and $\alpha = 1.95$. In the top right panel we show the density for the noise driving the system and in the lower right hand panel we show the Q-Q plot, as described in Sect. 4.1. Here we observe the appearance of slight positive drift whereas for purely stable noise [9] such drift was negative, and appeared at lower values of the Lévy index, for example $\alpha = 1.5$. Note that the density for the noise is barely distinguishable from the Gaussian case; it is only in the Q-Q plot, comparing the tempered stable noise to Gaussian noise, that the tail shows signs of weak deviation from the Gaussian. However, the deviation here is less than that visible in the corresponding plot in Fig.3 of [9], a consequence of tempering.

Decreasing the Lévy parameter down to $\alpha = 1.5$ we obtain the result shown in Fig.6 which exhibits a lower but still positive slope. This contrasts with a negative slope at this value of α for the purely stable noise (Fig.4 of [9]). Moreover in this tempered case we observe many more 'larger jumps' in the trajectories compared to $\alpha = 1.95$, however many trajectories seem to show a jump of less than π only to re-

turn down to the cluster. Noticeable in this sense is the orange coloured path in the left hand panel which nearly jumps 3π but then returns to the cluster at 2π shifted with respect to the lower group that have seen no jumps out of the basin at all. The density for the noise here is visibly different from the Gaussian with a stronger signal in the Q-Q plot showing the heavy tail in the positive direction.

In order to see how the drift is influenced by the tempering parameter we stay with $\alpha = 1.5$ and plot in Fig.7 the case of $\lambda = 0.1$ We observe clearly that the drift is now negative, not positive, with many more jumps close to but not exceeding π compared to the $\lambda = 0.2$ result. In addition, some (for example, the orange path in the left hand panel of Fig.6) jumps that for $\lambda = 0.2$ fell back into the basin are seen at the lower value of λ to finally succeed to jump out and rejoin 2π later (the light purple trajectory in the left hand panel of Fig.6).

We return to $\lambda = 0.2$ and decrease α down to $\alpha = 1.1$, as shown in Fig.8, and the paths also exhibit a negative drift. Remarkably, the densities for the noise for $\alpha = 1.5$ and 1.1 are qualitatively similar, as are the Q-Q plots. Thus there is no obvious correlation between the sign of the slope of the trajectories and the shape of the noise density. Other than the slope, a significant difference between these two cases is the proliferation of jumps close to but not exceeding π for the lower value of α, to which we shall return. We emphasise that this aligns with the property that in the associated Q-Q plots the the tempered stable distribution is close to the Gaussian around the value zero describing small jitters around zero in contrast to large jumps.

We now decrease below $\alpha = 1$ to $\alpha = 0.7$ in Fig.9 and the drift is strongly positive. The sign of the slope here is consistent with that for the stable case (Fig.5 in [9], however the tempered case shows far more synchronisation - fewer large jumps beyond π, and those that do jump outside the basin of attraction are fewer in between. Note that in the stable case, Fig.5 of [9], the density is shifted to the right with the mode of the distribution on the positive side of the vertical axis which goes hand-in-hand with the mean of the distribution in that case being divergent (due to the heavy tail). Here, tempering - because of softening of the positive tail to give a finite mean - causes the density to be closer to the centre, with the mode on the negative side now.

Finally, at $\lambda = 0.2$, we decrease to $\alpha = 0.5$ in Fig.10. This suggests reasonable levels of synchronisation but at lower drift than for $\alpha = 0.7$. We note that for the stable case at $\alpha = 0.5$ there was no semblance of order with a proliferation of large jumps (and thus we did not show a plot in [9] for this value). Tempering evidently has improved synchronisation at lower values of α, as already shown using the Fokker-Planck approach and in measuring the order parameter.

These last two cases bring into relief the mechanism we are proposing for improved synchronisation at low α. Observe in the Q-Q plots of Figs.9 and 10 that the tempered stable noise is close to the Gaussian around the origin, while it is locally depleted (the curve dips either below the dashed line or drops back to it) for intermediate negative values. These should be contrasted with the Q-Q plot in Fig.5 of [9] which shows the stable noise strongly heavy in the tails and depleted around the origin. This manifests our statement that for $\alpha < 1$ tempering softens the tails while depleting intermediate regions of the probability density so that the noise is dominated by very small fluctuations. The value of the tempering constant λ thus influences the slope of the induced drift whereby now those oscillators that may undertake a large jump, of the order of π, may still not leave the basin of attraction. Tempering thus introduces a third class of oscillators, over and above the separation discussed in [9] of 'large' and 'non-jumpers', namely those undergoing intermediate scale jumps to the boundary, but not beyond, of the basin of attraction. The proportion of these change with varying α and λ such that the slope of the drift changes in order to respect the overall finite mean overall for the noise.

5. Conclusions

We have examined the dynamics of identical Kuramoto oscillators under tempered stable Lévy noise, further generalising numerous studies of the stochastic model from Brownian white noise models. Some of the results were entirely predictable: tempering with constant $\lambda > 0$ leads to improved synchronisation compared to the behaviour under noise for the same values of coupling κ, noise strength σ and Lévy index α. Also, the Barabasi-Alberts scale free graph degrades more gracefully in synchronisation under increased noise strength compared to the Erdos-Renyi random graph; the hub in scale-free graphs provides robustness to oscillator dynamics across a wide variety of noise models. Some results were surprising: for fixed coupling, noise strength and tempering constant the collective synchronisation improved with decreasing α. Also, the direc-

tion of the induced drift of oscillators was dependent on the values of α, σ, β and λ in a more complicated manner than might have been expected from the stable case. These behaviours could be analytically computed by solving the tempered fractional Fokker-Planck equation for probability distributions of Laplacian modes after linearising close to synchrony. And, finally, a simple intuition for these behaviours could be built once the specifics of changes in the probability densities of tempered stable noise were appreciated, specifically the narrowing of densities around the mode for $\alpha < 1$.

Acknowledgments

One of us (ACK) is supported through a Chief Defence Scientist Fellowship and expresses gratitude for the hospitality of ANU. We are grateful for discussions with Mathew Zuparic, Markus Brede and Richard Taylor.

[1] Y. Kuramoto, Chemical oscillations, waves and turbulence. 1984, Berlin: Springer, 2008.
[2] J. A. Acebrón, L. L. Bonilla, C. J. P. Vicente, F. Ritort, R. Spigler, The Kuramoto model: A simple paradigm for synchronization phenomena, Reviews of Modern Physics 77 (1) 137.
[3] S. N. Dorogovtsev, A. V. Goltsev, J. F. Mendes, Critical phenomena in complex networks, Reviews of Modern Physics 80 (4) 1275.
[4] A. Arenas, A. Díaz-Guilera, J. Kurths, Y. Moreno, C. Zhou, Synchronization in complex networks, Physics Reports 469 (3) (2008) 93–153.
[5] F. Dörfler, F. Bullo, Synchronization in complex networks of phase oscillators: A survey, Automatica 50 (6) (2014) 1539–1564.
[6] B. C. Bag, K. Petrosyan, C.-K. Hu, Influence of noise on the synchronization of the stochastic Kuramoto model, Physical Review E 76 (5) 056210.
[7] H. Khoshbakht, F. Shahbazi, K. A. Samani, Phase synchronization on scale-free and random networks in the presence of noise, Journal of Statistical Mechanics: Theory and Experiment 2008 (10) 10020.
[8] R. K. Esfahani, F. Shahbazi, K. A. Samani, Noise-induced synchronization in small world networks of phase oscillators, Physical Review E 86 (3) 036204.
[9] A. C. Kalloniatis, D. O. Roberts, Synchronisation of networked Kuramoto oscillators under stable Lévy noise, Physica A: Statistical Mechanics and its Applications 466 (2017) 476–491.
[10] D. M. Abrams, H. A. Yaple, R. J. Wiener, Dynamics of social group competition: modeling the decline of religious affiliation, Physical Review Letters 107 (8) 088701.
[11] J. C. González-Avella, M. G. Cosenza, M. San Miguel, Localized coherence in two interacting populations of social agents, Physica A: Statistical Mechanics and its Applications 399 (2014) 24–30.
[12] A. Pluchino, S. Boccaletti, V. Latora, A. Rapisarda, Opinion dynamics and synchronization in a network of scientific collaborations, Physica A: Statistical Mechanics and its Applications 372 (2) (2006) 316–325.
[13] A. C. Kalloniatis, M. L. Zuparic, Fixed points and stability in the two-network frustrated Kuramoto model, Physica A: Statistical Mechanics and its Applications 447 (2016) 21–35.
[14] U. Neisser, Cognition and reality: Principles and implications of cognitive psychology., WH Freeman/Times Books/Henry Holt & Co, 1976.
[15] R. Ratcliff, G. McKoon, The diffusion decision model: theory and data for two-choice decision tasks, Neural Computation 20 (4) (2008) 873–922.
[16] H. W. Rittel, M. M. Webber, Dilemmas in a general theory of planning, Policy Sciences 4 (2) (1973) 155–169.
[17] C. K. Morewedge, D. Kahneman, Associative processes in intuitive judgment, Trends in Cognitive Sciences 14 (10) (2010) 435–440.
[18] G. Klein, V. M. Chase, Sources of power: How people make decisions, Nature 392 (6673) (1998) 242–242.
[19] J. A. Roberts, T. W. Boonstra, M. Breakspear, The heavy tail of the human brain, Current Opinion in Neurobiology 31 (2015) 164–172.
[20] H. Hong, M.-Y. Choi, B. J. Kim, Synchronization on small-world networks, Physical Review E 65 (2) 026139.
[21] T. Ichinomiya, Frequency synchronization in a random oscillator network, Physical Review E 70 (2) (2004) 026116.
[22] A. Dekker, Realistic social networks for simulation using network rewiring, in: International Congress on Modelling and Simulation, 2007, pp. 677–683.
[23] J. G. Restrepo, E. Ott, B. R. Hunt, Approximating the largest eigenvalue of network adjacency matrices, Physical Review E 76 (5) (2007) 056119.
[24] E. Oh, D.-S. Lee, B. Kahng, D. Kim, Synchronization transition of heterogeneously coupled oscillators on scale-free networks, Physical Review E 75 (1) 011104.
[25] J. Gómez-Gardeñes, Y. Moreno, A. Arenas, Synchronizability determined by coupling strengths and topology on complex networks, Physical Review E 75 (6) 066106.
[26] H. Sakaguchi, Y. Kuramoto, A soluble active rotater model showing phase transitions via mutual entertainment, Progress of Theoretical Physics 76 (3) 576.
[27] K. Sato, Lévy processes and infinite divisibility, Cambridge University Press Cambridge, 1999.
[28] R. Taylor, There is no non-zero stable fixed point for dense networks in the homogeneous Kuramoto model, Journal of Physics A: Mathematical and Theoretical 45 (5) 055102.
[29] F. R. K. Chung, Spectral graph theory, Vol. 92, American Mathematical Soc., 1997.
[30] K.-I. Sato, M. Yamazato, Operator-self-decomposable distributions as limit distributions of processes of Ornstein-Uhlenbeck type, Stochastic Process. Appl. 17 (1) (1984) 73–100.
[31] B. Bollobás, Modern Graph Theory, Springer-Verlag, New York, 1998.
[32] A. Arenas, A. Díaz-Guilera, C. J. Pérez-Vicente, Synchronization reveals topological scales in complex networks, Physical Review Letters 96 (11) 114102.
[33] A. C. Kalloniatis, From incoherence to synchronicity in the network Kuramoto model, Physical Review E 82 (6) 066202.
[34] P. N. McGraw, M. Menzinger, Laplacian spectra as a diagnostic tool for network structure and dynamics, Physical Review E 77 (3) 031102.
[35] S. Jespersen, R. Metzler, H. C. Fogedby, Lévy flights in external force fields: Langevin and fractional Fokker-Planck equations and their solutions, Physical Review E 59 (3) 2736.
[36] R. Kawai, H. Masuda, On simulation of tempered stable random variates, Journal of Computational and Applied Mathematics 235 (8) (2011) 2873–2887.

[37] A. Kullberg, D. del Castillo-Negrete, Transport in the spatially tempered, fractional Fokker–Planck equation, Journal of Physics A: Mathematical and Theoretical 45 (25) 255101.
[38] M. L. Zuparic, A. C. Kalloniatis, Stochastic (in)stability of synchronisation of oscillators on networks, Physica D: Nonlinear Phenomena 255 (2013) 35–51.
[39] B. Baeumer, M. M. Meerschaert, Tempered stable lévy motion and transient super-diffusion, Journal of Computational and Applied Mathematics 233 (10) (2010) 2438–2448.

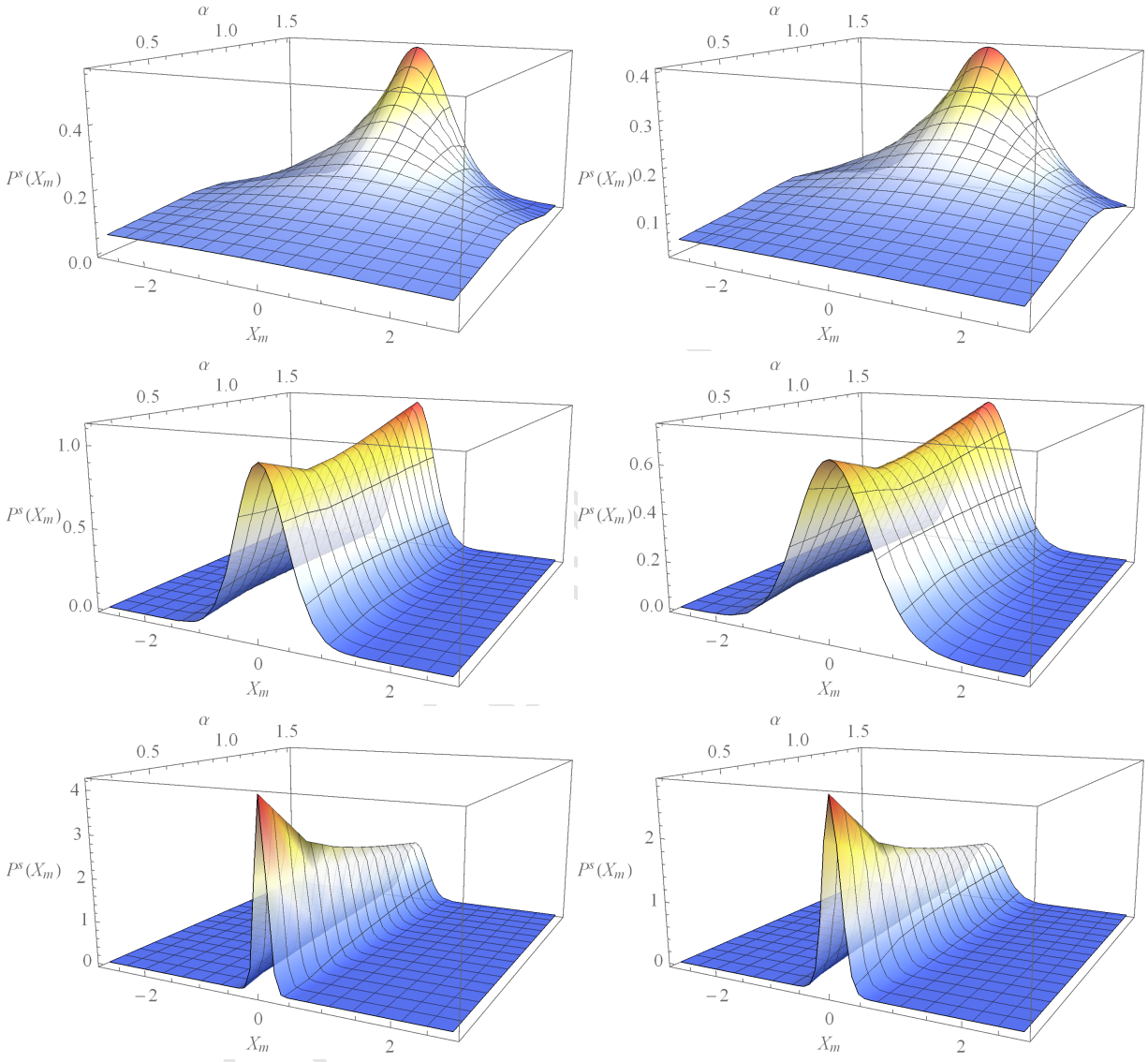

Figure 3: Solutions to the steady-state fractional Fokker-Planck equation for different α, comparing $\lambda = 0.01$ (top), $\lambda = 0.2$ (middle) and $\lambda = 1$ (bottom) for the $m = 1$ mode at $\sigma = 3$. Left hand column is for the BA graph and right hand column the ER graph.

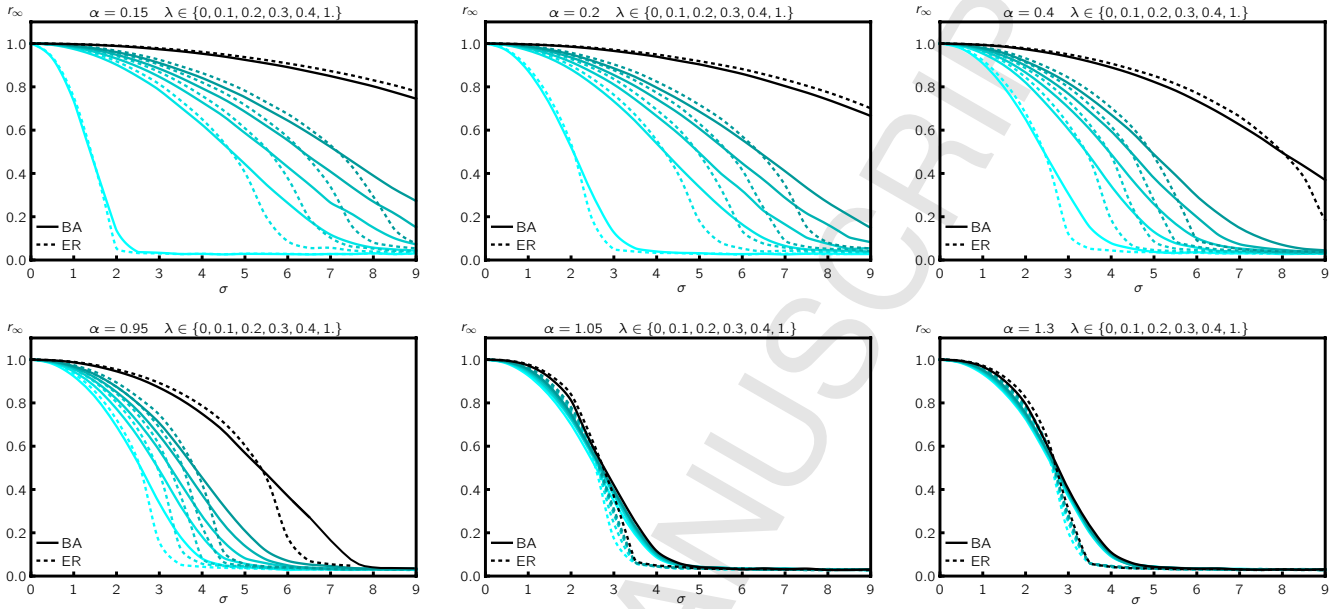

Figure 4: Plots of the asymptotic value of the order parameter, r_∞ (averaged over 30 graphs and 128 paths) versus σ for the BA (solid line) and ER (dashed line) graphs at various α and λ. Here we select specific values of α between 0 and 2 going from left to right and top to bottom, with different values of λ indicated in shades of cyan running from light ($\lambda = 0$) to black ($\lambda = 1$).

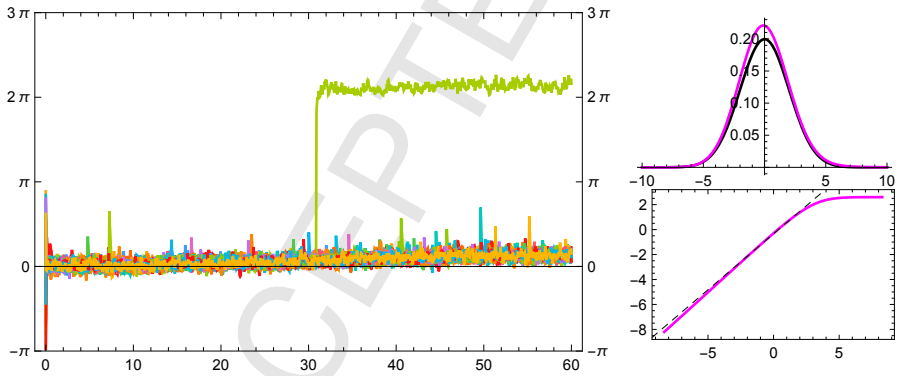

Figure 5: Simulation of one path of $N = 1000$ Kuramoto $\omega_i = 0$ oscillators in Eq.(1) at $K = N$ on an ER network subject to tempered stable Lévy noise with $\alpha = 1.95, \lambda = 0.05, \sigma = 2$, plotting 30 individual θ_i as functions of t. The probability density functions of this choice of noise (purple curve) and the Gaussian noise (black curve) are shown top right. The Q-Q plot (bottom right) compares the tempered stable Lévy noise against the Gaussian noise. We note that this figure looks similar to the result in [9] as with small λ and $\alpha = 1.95$, the result is nearly indistinguishable from the stable case.

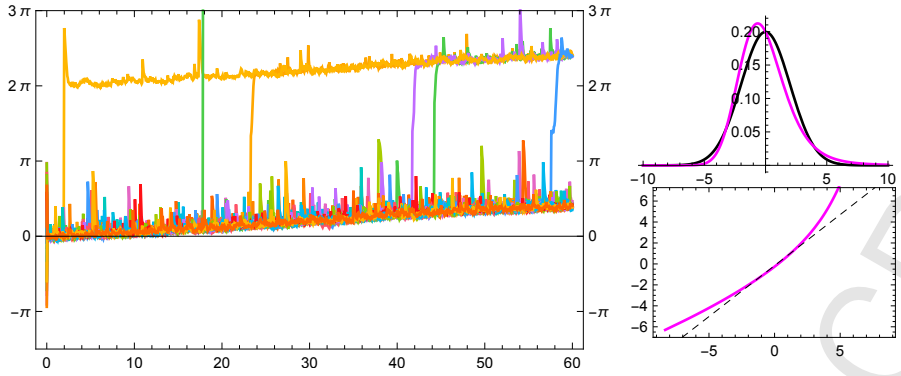

Figure 6: Simulation of one path of $N = 1000$ Kuramoto $\omega_i = 0$ oscillators in Eq.(1) at $K = N$ on an ER network subject to tempered stable Lévy noise with $\alpha = 1.5, \lambda = 0.2, \sigma = 2$, plotting 30 individual θ_i as functions of t. The probability density functions of this choice of noise (purple curve) and the Gaussian noise (black curve) are shown top right. The Q-Q plot (bottom right) compares the tempered stable Lévy noise against the Gaussian noise.

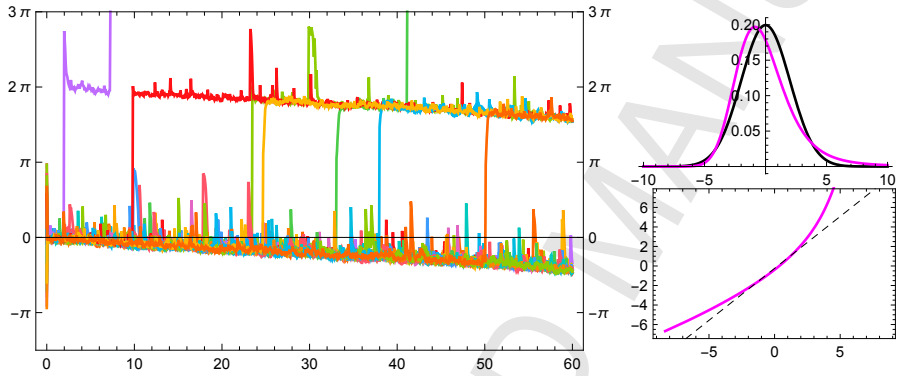

Figure 7: Simulation of one path of $N = 1000$ Kuramoto $\omega_i = 0$ oscillators in Eq.(1) at $K = N$ on an ER network subject to tempered stable Lévy noise with $\alpha = 1.5, \lambda = 0.1, \sigma = 2$, plotting 30 individual θ_i as functions of t. The probability density functions of this choice of noise (purple curve) and the Gaussian noise (black curve) are shown top right. The Q-Q plot (bottom right) compares the tempered stable Lévy noise against the Gaussian noise.

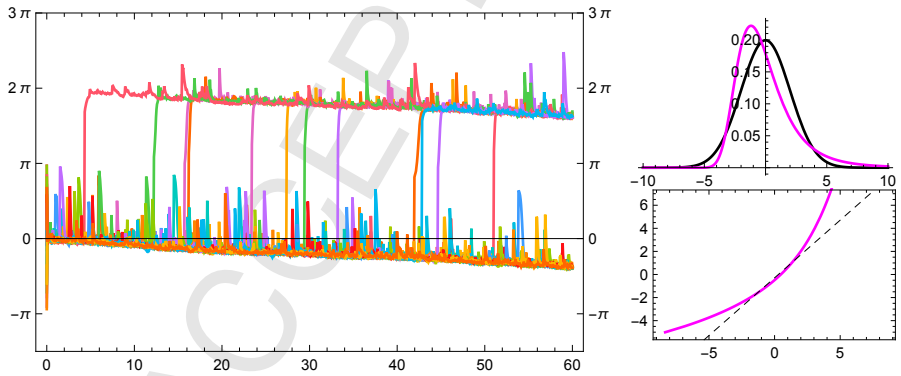

Figure 8: Simulation of one path of $N = 1000$ Kuramoto $\omega_i = 0$ oscillators in Eq.(1) at $K = N$ on an ER network subject to tempered stable Lévy noise with $\alpha = 1.1, \lambda = 0.2, \sigma = 2$, plotting 30 individual θ_i as functions of t. The probability density functions of this choice of noise (purple curve) and the Gaussian noise (black curve) are shown top right. The Q-Q plot (bottom right) compares the tempered stable Lévy noise against the Gaussian noise.

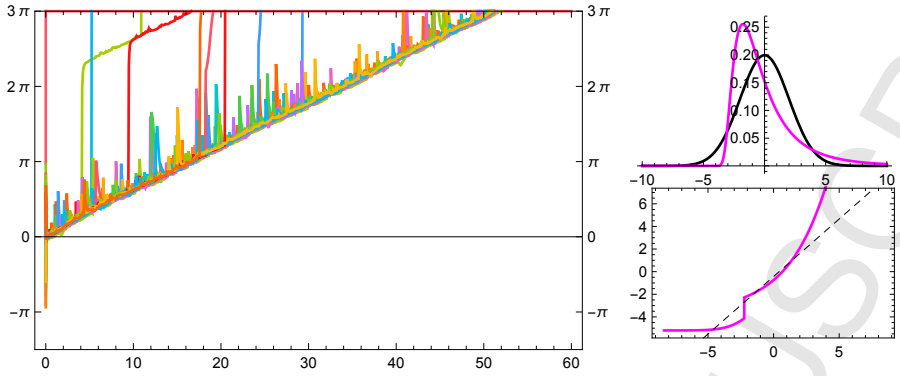

Figure 9: Simulation of one path of $N = 1000$ Kuramoto $\omega_i = 0$ oscillators in Eq.(1) at $K = N$ on an ER network subject to tempered stable Lévy noise with $\alpha = 0.7, \lambda = 0.2, \sigma = 2$, plotting 30 individual θ_i as functions of t. The probability density functions of this choice of noise (purple curve) and the Gaussian noise (black curve) are shown top right. The Q-Q plot (bottom right) compares the tempered stable Lévy noise against the Gaussian noise.

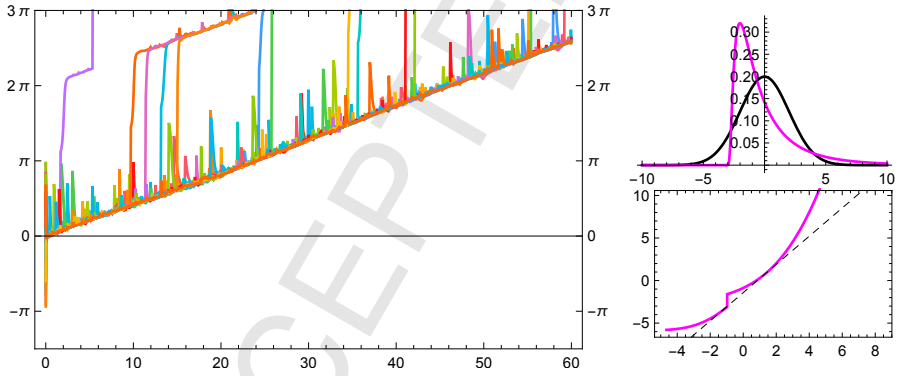

Figure 10: Simulation of one path of $N = 1000$ Kuramoto $\omega_i = 0$ oscillators in Eq.(1) at $K = N$ on an ER network subject to tempered stable Lévy noise with $\alpha = 0.5, \lambda = 0.2, \sigma = 2$, plotting 30 individual θ_i as functions of t. The probability density functions of this choice of noise (purple curve) and the Gaussian noise (black curve) are shown top right. The Q-Q plot (bottom right) compares the tempered stable Lévy noise against the Gaussian noise.

Highlights

1. We apply tempered stable Levy noise to the Kuramoto model of equal frequency oscillators.
2. Barabasi-Alberts and Erdos-Renyi random network cases of 1000 nodes are compared.
3. Differences in synchronisation for the two cases generalise beyond Gaussian noise.
4. New types of synchrony are seen showing drift depending on noise parameters.
5. The results are analytically explained with the fractional Fokker-Planck equation.